Computational predictions of damage propagation preceding dissection of ascending thoracic aortic aneurysms

S. Jamaleddin Mousavi, Solmaz Farzaneh, Stéphane Avril

Computational predictions of damage propagation preceding dissection of ascending thoracic aortic aneurysms

S. Jamaleddin Mousavi, Solmaz Farzaneh and Stéphane Avril

affiliations: [1]Mines Saint-Étienne, Univ Lyon, Univ Jean Monnet, INSERM, U 1059 Sainbiose, Centre CIS, F - 42023 Saint-Étienne France.

abbreviated title: Patient–specific predictions of aneurysm growth and remodeling

correspondence: *Stéphane Avril, Mines Saint-Étienne, Univ Lyon, Univ Jean Monnet, INSERM, U 1059 Sainbiose, Centre CIS, F - 42023 Saint-Étienne France.
Phone: 0477420188, Fax: +33477420000, e-mail: avril@emse.fr

Abstract

Dissections of ascending thoracic aortic aneurysms (ATAA) cause significant morbidity and mortality worldwide. They occur when a tear in the intima-media of the aorta permits the penetration of the blood and the subsequent delamination and separation of the wall in two layers, forming a false channel. In order to predict computationally the risk of tear formation, stress analyses should be performed layer-specifically and they should consider internal or residual stresses which exist in the tissue. In the present paper, we propose a novel layer–specific damage model based on the constrained mixture theory (CMT) which intrinsically takes into account these internal stresses and which can predict appropriately the tear formation. The model is implemented in finite-element commercial software Abaqus coupled with user material subroutine (UMAT). Its capability is tested by applying it to the simulation of different exemplary situations, going from *in vitro* bulge-inflation experiments on aortic samples to *in vivo* over-pressurizing of patient-specific ATAAs. The simulations reveal that damage correctly starts from the intimal layer (luminal side) and propagates across the media as a tear, but never hits the adventitia. This scenario is typically the first stage of development of an acute dissection, which is predicted for pressures of about 2.5 times the diastolic pressure by the model after calibrating the parameters against experimental data carried out on collected ATAA samples. Further validations on a larger cohort of patients should hopefully confirm the potential of the model in predicting patient-specific damage evolution and possible risk of dissection during aneurysm growth for clinical applications.

keywords: layer-specific damage model; constrained mixture theory; residual stresses; anisotropic behaviour; uni- and biaxial tests; patient specific over–pressurizing

1 Introduction

Rupture of aortic aneurysms is the cause of significant morbidity and mortality; it causes the death of 30,000 people in Europe and 15,000 people in the United States every year [71, 77] including at least 10–20% ascending thoracic aortic aneurysms (ATAA). Thanks to many advances in biomechanics, medical imaging, surgical techniques, genetics and cell biology, it is currently

known that remodeling of the aortic wall is essential in ATAA before the onset of damage and eventual rupture, which occurs when the peak wall stress exceeds the strength [83].
The aortic wall comprises different layers with specific compositions. The media harbors smooth muscle cells (SMCs) embedded between lamellas made mostly of elastin and collagen. The adventitia harbors fibroblasts in a collagenous structure made mostly of bundles of collagen. Their mechanical behaviour under cyclic uniaxial or biaxial tests shows inelastic effects such as the Mullins effect, permanent set, deformation-induced anisotropy, and hysteresis [33]. Many tensile tests have been carried out on human aortas to explore their mechanical and rupture behavior since the pioneering work of Mohan and Melvin on flatten dumbbell aortic specimens [60]. Vorp et al. [83] observed a significant decrease in the tensile strength of ATAA specimens and concluded that the formation of ATAA was accompanied by weakening and stiffening of the aortic wall. In contrast, García-Herrera et al. [38] did not find major differences between the mechanical strength of aneurysms and healthy tissues in uniaxial tensile tests. They concluded that the age factor is a significant reason for the variations of rupture stress and stretch. Findings of Duprey et al. [29] indicated that the aortic wall is significantly anisotropic, the axial direction being weaker than the circumferential one.
An important aspect of the biomechanical behavior of arteries is the permanent state of biaxial tensile stresses that exist *in vivo*. Although uniaxial tensile tests are easier to achieve, they are not the most proper methodology to evaluate tissue anisotropy and rupture. Biaxial tests are more appropriate to determine if the tissue shows different properties between the axial and circumferential directions. An appropriate alternative to investigate the biaxial mechanical behavior of the arterial walls can be bulge inflation technique [54, 58, 61, 73, 30]. Quasi-static bulge inflation tests of Mohan and Melvin [61] on 16 healthy descending aortas demonstrated that the rupture of aortic tissue is always oriented in the circumferential direction. This is consistent with the results of Marra et al. [58] obtained from inflation tests on porcine healthy aortic tissues. Inflation tests using ATAA specimens were recently carried out by Duprey et al. [30] up to rupture. They derived for all the samples the average Cauchy stress at which the rupture occurred. Although the implementation of such a setup needs significant expertise, the application of advanced digital imaging techniques allowed to simultaneously assess the localized stress in the area that eventually ruptures [30] and the material parameters for constitutive numerical modeling purposes [25, 24].

In all these experiments, an important issue was always to be able to localize the rupture of the tissue from its first initiation, especially when only one layer of the wall is concerned.
To address such issue, numerical models of arterial walls, based on an appropriate finite element (FE) damage model, can be very helpful. Over the last decades, many phenomenological and micromechanical models have been proposed to predict the damage evolution in soft [1, 7, 21, 22, 33] and hard [32, 41] tissues. The first damage model of soft tissues can be traced back to the 1970s [17]. More than three decades ago, Simo [75] presented a damage model for finite deformations. It was basically based on the multiplicative decomposition of the deformation gradient into a isochoric (volume-preserving) and a volumetric part in which damage only affects the former. Recently, damage models with a volumetric-deviatoric decoupling have been introduced to model the behavior of fibrous soft biological tissues [7, 21, 22, 33]. The fact that damage is applied only on the deviatoric part of the model means that, for a completely damaged structure, a volumetric quasi-incompressible undamaged part will always remain.
Damage models can be categorized in three groups: (i) deterministic models in which a pseudoelastic strain energy function with a few parameters or damage variables of continuum damage mechanics is employed to characterize the softening/damage effect, either isotropically [32, 81] or anisotropically [56, 80, 84]; (ii) probabilistic models in which probabilistic damage process and/or fiber recruitment can be included [43, 74]; (iii) micro–structural–based damage models of collagen fibers in which the microscopic damage behavior of individual collagen fibrils is considered and homogenized macroscopically [39]. All these formulations can be categorized as non-local [33] or local [1, 7, 21, 22, 41, 32] damage models. In the non–local methodologies an integral-type non-local averaging scheme is employed in the constitutive equations in order to limit the localization phenomena of damage variables and to overcome the mesh pathology. In contrast, in local approaches it is needed to introduce the energy dissipation as an element-size-dependent material property to solve such issue.
To the best of our knowledge, no numerical model about the inelastic behaviour of soft tissues considered layer-specific damage evolution with layer-specific *in situ* stresses. These *in situ* stresses are well evidenced when arteries are excised during a surgical intervention for instance. Due to the cancellation of *in vivo* loadings, the artery experiences an elastic recoiling [19, 49]. The layer-specificity of *in situ* stresses make internal or residual

stresses appear in the tissue even when the loading is removed. An effect of these internal stresses can be observed in arteries with the well–known open angle experiment [8, 37, 49]. Residual stresses can be observed in most of soft tissues [57, 87], including myocardium [42, 65, 85] and mitral leaflets [70]. The intrinsic reason of this specific mechanical behavior of soft tissues is their composite nature combined with different kinetics of growth and remodeling for each micro–constituent. For arteries, the different nature of the media and the adventitia is at the origin of a layer-specific stress distribution *in vivo*.
Our objective here is to develop a damage model based on the constrained mixture theory (CMT), taking into account the results of layer-specific mechanobiology occurring in the arterial wall. After introducing the model and its finite-element implementation, we show different simulations of damage initiation, going from *in vitro* experiments on aortic samples to over-pressurizing of a patient-specific ATAA.

2 Materials and Methods

2.1 Constitutive constrained mixture theorem based formulation

A computational FE model based on the constrained mixture theory [8, 15, 63] is developed to couple the failure of the heterogeneous arterial layers to the complex evolution of damage occurring at the microscopic structure. For a continuum body (here mixture), let $\boldsymbol{\chi} : \boldsymbol{\Omega}_0$ be the general mapping in a $\mathbb{R}^3$ domain. The deformation gradient $\mathbf{F}$ between a material point from a reference configuration $\mathbf{X} \in \boldsymbol{\Omega}_0$ and a position into a deformed configuration $\mathbf{x} = \boldsymbol{\chi}(\mathbf{X}, t) \in \boldsymbol{\Omega}$ at time t can be defined as

$$\mathbf{F}(\mathbf{X}, t) = \frac{\partial \boldsymbol{\chi}(\mathbf{X}, t)}{\partial \mathbf{X}} \tag{1}$$

At each layer of the arterial wall, a specific constitutive energy function is assumed for each constituent with contribution of its own mass fraction. To define a homeostatic state at physiological pressure and axial stretch (considered as a clinically and biologically relevant reference configuration), the concept of constituent-specific deposition stretches is employed. Soft tissues

are known to be highly deformable, yet they experience negligible volume changes. For many applications, their behaviour can be described with decoupled quasi-incompressible hyperelastic models, damage affecting solely the deviatoric term [68, 12]. The fact that damage is assumed only in the deviatoric part of the model means that, for a completely damaged structure, a volumetric quasi-incompressible contribution will remain undamaged. Thus, considering Continuum Damage Mechanics (CDM), a damaged material is characterized by voids resulting in a loss of the stiffness and strength of each constituent of the mixture [27, 32]. Moreover, we assume there are no damage occurring in the SMC contribution. Considering these features and consistently with the CMT, it is assumed that the strain energy function (SEF) of the arterial wall is a mass averaged function, consequently, the total specific Helmholtz free energy function can be written as

$$\begin{aligned} W =&(1-D^{\mathrm{e}})\rho^{\mathrm{e}}\overline{W}^{\mathrm{e}}(\overline{I}_1^{\mathrm{e}})+ \\ &\sum_{i=1}^{n}(1-D^{\mathrm{c}_i})\rho^{\mathrm{c}_i}\overline{W}^{\mathrm{c}_i}(\overline{I}_4^{\mathrm{c}_i})+ \\ &\rho^{\mathrm{m}}\overline{W}^{\mathrm{m}}(\overline{I}_4^{\mathrm{m}})+U(J) \end{aligned} \tag{2}$$

where superscripts e, c_i and m represent respectively the elastin fiber constituent, the constituent made of each of the n possible collagen fiber families and the SMC constituent, all these constituents constituting the mixture. In Eq. 2, $D^j \in [0,1]$ is the damage parameter (D^j =0 and D^j =1 indicate undamaged and completely damaged constituent, respectively), ρ^j stands for mass fraction, $\overline{W}^j$ the deviatoric or volume-preserving part of the free energy of intact constituents, depending on the first ($\overline{I}_1^j$) and fourth ($\overline{I}_4^j$) invariants of the related constituents of the mixture ($j \in \{\mathrm{e}, \mathrm{c}_i, \mathrm{m}\}$). $U(J)$ is the volumetric contribution of the total free energy. The SEF of elastin constituent is described by a Neo-Hookean strain energy function such as [15, 28, 46]

$$\overline{W}^{\mathrm{e}}(\overline{I}_1^{\mathrm{e}}) = \mu^{\mathrm{e}}(\overline{I}_1^{\mathrm{e}} - 3) \tag{3}$$

where μ^{e} is a stress-like material parameter. The first invariants of the deviatoric Cauchy–Green deformation tensor is introduced as

$$\begin{aligned} \overline{I}_1^{\mathrm{e}} &= tr(\overline{\mathbf{C}}^{\mathrm{e}}) \\ \overline{\mathbf{C}}^{\mathrm{e}} &= \overline{\mathbf{F}}^{\mathrm{e}\mathrm{T}}\overline{\mathbf{F}}^{\mathrm{e}} \end{aligned} \tag{4}$$

with the deviatoric part of the deformation gradient in the elastin constituent and the volume ratio, J, as

$$\begin{aligned}\overline{\mathbf{F}}^{\mathrm{e}} &= J^{\mathrm{e}(-1/3)}\mathbf{F}^{\mathrm{e}}\\ \mathbf{F}^{\mathrm{e}} &= \mathbf{F}\mathbf{G}_h^{\mathrm{e}}\\ J^{\mathrm{e}} &= \det(\mathbf{F}^{\mathrm{e}})\end{aligned} \tag{5}$$

where $\mathbf{G}_h^{\mathrm{e}}$ is the constituent-specific deposition stretch of the elastin constituent with respect to the reference configuration [8, 15].
The mechanical behavior of collagen, including the passive contribution of SMCs, is respectively described using an exponential expression as in [8, 15, 71, 72]:

$$\begin{aligned}\overline{W}^{\mathrm{c}_i}(\overline{I}_4^{\mathrm{c}_i}) &= \frac{k_1^{\mathrm{c}_i,\mathrm{t}}}{2k_2^{\mathrm{c}_i,\mathrm{t}}}\left[e^{\left(k_2^{\mathrm{c}_i,\mathrm{t}}(\overline{I}_4^{\mathrm{c}_i}-1)^2\right)}-1\right], \text{ under tension}\\ \overline{W}^{\mathrm{c}_i}(\overline{I}_4^{\mathrm{c}_i}) &= \frac{k_1^{\mathrm{c}_i,\mathrm{c}}}{2k_2^{\mathrm{c}_i,\mathrm{c}}}\left[e^{\left(k_2^{\mathrm{c}_i,\mathrm{c}}(\overline{I}_4^{\mathrm{c}_i}-1)^2\right)}-1\right], \text{ under compression}\end{aligned} \tag{6}$$

and

$$\begin{aligned}\overline{W}^{\mathrm{m}}(\overline{I}_4^{\mathrm{m}}) &= \frac{k_1^{\mathrm{m},\mathrm{t}}}{2k_2^{\mathrm{m},\mathrm{t}}}\left[e^{\left(k_2^{\mathrm{m},\mathrm{t}}(\overline{I}_4^{\mathrm{m}}-1)^2\right)}-1\right], \text{ under tension}\\ \overline{W}^{\mathrm{m}}(\overline{I}_4^{\mathrm{m}}) &= \frac{k_1^{\mathrm{m},\mathrm{c}}}{2k_2^{\mathrm{m},\mathrm{c}}}\left[e^{\left(k_2^{\mathrm{m},\mathrm{c}}(\overline{I}_4^{\mathrm{m}}-1)^2\right)}-1\right], \text{ under compression}\end{aligned} \tag{7}$$

where k_1 and k_2 with superscripts c_i and m are stress-like and dimensionless material parameters of the collagen and SMCs contributions, respectively. It is noteworthy that those can take different values when fibers are under compression or tension denoted by t and c in Eqs. 6 and 7 [10]. $\overline{I}_4^{\mathrm{c}_i} = J^{\mathrm{c}_i(-2/3)}I_4^{\mathrm{c}_i}$ and $\overline{I}_4^{\mathrm{m}} = J^{\mathrm{m}(-2/3)}I_4^{\mathrm{m}}$ which are less than one when fiber is under compression and greater than one when fiber is under tension. $J^{\mathrm{c}_i} = \det(\mathbf{F}^{\mathrm{c}_i})$ and $J^{\mathrm{m}} = \det(\mathbf{F}^{\mathrm{m}})$ are corresponding Jacobians. Noting that $I_4^{\mathrm{c}_i}$ and I_4^{m} are the fourth invariants of collagen and SMCs contributions which can be written as:

$$I_4^{\mathrm{c}_i} = G_h^{\mathrm{c}_i 2}\mathbf{C} : \mathbf{M}^{\mathrm{c}_i} \otimes \mathbf{M}^{\mathrm{c}_i} \tag{8}$$

$$I_4^{\mathrm{m}} = G_h^{\mathrm{m}2}\mathbf{C} : \mathbf{M}^{\mathrm{m}} \otimes \mathbf{M}^{\mathrm{m}} \tag{9}$$

with

$$\mathbf{C} = \mathbf{F}^{\mathrm{T}}\mathbf{F} \tag{10}$$

being the right Cauchy-Green stretch tensor of the arterial wall mixture.

$G_h^{\mathrm{c}_i}$ and G_h^{m} are the specific deposition stretches of each collagen fiber family and SMCs with respect to the reference configuration, respectively. $\mathbf{M}^{\mathrm{c}_i}$ and $\mathbf{M}^{\mathrm{c}_i}$ are the unit vectors along the dominant orientation of anisotropy in the reference configuration for each family of collagen fibers and of SMCs, respectively. For the ith family of collagen fibers $\mathbf{M}^{\mathrm{c}_i} = [0 \ \sin\alpha^i \ \cos\alpha^i]$, where α^i is the angle of the ith family of collagen fibers with respect to the axial direction. It is assumed that $\mathbf{M}^m$ coincides with the circumferential direction of the vessel in the reference configuration [8, 15].

The volumetric contribution of the SEF can be described as [71]:

$$U(J) = \kappa(J-1)^2 \tag{11}$$

where κ is the bulk modulus and $J = \det(\mathbf{F})$ is the Jacobian.
Referring to Eq. 2 leads to the expression of the second Piola-Kirchhoff stress tensor as:

$$\mathbf{S} = (1-D^{\mathrm{e}})\overline{\mathbf{S}}^{\mathrm{e}} + \sum_{i=1}^{n}(1-D^{\mathrm{c}_i})\rho^{\mathrm{c}_i}\overline{\mathbf{S}}^{\mathrm{c}_i} + \rho^{\mathrm{m}}\overline{\mathbf{S}}^{\mathrm{m}} + \mathbf{S}_{vol} \tag{12}$$

where $\overline{\mathbf{S}}^j = 2\frac{\partial \overline{W}^j}{\partial \mathbf{C}}$ is the second Piola-Kirchhoff stress of corresponding undamaged constituents of the mixture, $(j \in \{\mathrm{e}, \mathrm{c}_i, \mathrm{m}\})$, and $\mathbf{S}_{vol} = Jp\mathbf{C}^{-1}$ with $p = \frac{\mathrm{d}U}{\mathrm{d}J}$, the hydrostatic pressure. The Cauchy stress tensor is derived from the second Piola-Kirchoff stress as [46, 45]

$$\boldsymbol{\sigma} = J^{-1}\mathbf{F}\mathbf{S}\mathbf{F}^{\mathrm{T}} \tag{13}$$

The material tangent constitutive tensor implemented in the model is given by

$$\begin{aligned}\mathbb{C} =& \rho^{\mathrm{e}}\left[(1-D^{\mathrm{e}})\overline{\mathbb{C}}^{\mathrm{e}} - \frac{1}{\psi^{\mathrm{e}}}\frac{\partial D^{\mathrm{e}}}{\partial \psi^{\mathrm{e}}}\overline{\mathbf{S}}^{\mathrm{e}} \otimes \overline{\mathbf{S}}^{\mathrm{e}}\right] + \\ & \sum_{i=1}^{n}\rho^{\mathrm{c}_i}\left[(1-D^{\mathrm{c}_i})\overline{\mathbb{C}}^{\mathrm{c}_i} - \frac{1}{\psi^{\mathrm{c}_i}}\frac{\partial D^{\mathrm{c}_i}}{\partial \psi^{\mathrm{c}_i}}\overline{\mathbf{S}}^{\mathrm{c}_i} \otimes \overline{\mathbf{S}}^{\mathrm{c}_i}\right] + \\ & \rho^{\mathrm{m}}\overline{\mathbb{C}}^{\mathrm{m}} + \mathbb{C}_{vol}\end{aligned} \tag{14}$$

where $\overline{\mathbb{C}}^j = 4\frac{\partial \overline{W}^j}{\partial \mathbf{C}}$ corresponds to the material elasticity tensor of undamaged (virgin) material. ψ is Simo and Ju [75] energetic norm and $\frac{\partial D^j}{\partial \psi}$, $(j \in \{\mathrm{e}, \mathrm{c}_i\})$

is the derivation of the damage function with respect to the energetic norm that will be introduced in the next section. The volumetric part of the constitutive tensor, $\mathbb{C}_{vol}$, is given by

$$\mathbb{C}_{vol} = 2p\frac{\partial(J\mathbf{C}^{-1})}{\partial\mathbf{C}} + 2J\mathbf{C}^{-1} \otimes p\frac{\partial p}{\partial\mathbf{C}} \tag{15}$$

2.2 Constitutive formulation of damage evolution

The damage model here is formulated in agreement with the principles of CDM applied in many mechanobiological studies [27, 31, 32]. Therefore, it is assumed that apparent density of damage evolves with mechanical loadings. So, for the evolution of the damage variable, a linear softening law is employed as described in [31]

$$\begin{aligned} D^j &= G^j(\psi^j) = \frac{1 - \frac{\psi_0^j}{\psi^j}}{1 + H^j} \\ H^j &= -\frac{{\psi_0^j}^2}{2\omega^j}; \omega^j = \frac{\Omega^j}{L_0} \\ \psi^j &= \sqrt{2\overline{W}^j} \end{aligned} \tag{16}$$

where $j \in \{\mathrm{e}, \mathrm{c}_i\}$ while ψ_0^j is the initial damage threshold and ω^j represents the fracture energy per unit volume which depends on the maximum dissipated fracture energy per unit of area, Ω^j, and on the element size in the reference configuration, L_0. The dependence on the element size is aimed at overcoming the mesh pathology. As damage–localized elements are increasingly damaged the stiffness of their deviatoric part decreases so that they become largely deformed. The quasi–incompressible character of the hybrid elements requires that the adjacent band of elements deforms to accommodate the narrowing of the highly damaged elements. This, in turn, generates higher deviatoric stresses in this adjacent row of elements, which results in damage initiation [64].

Finally, for calculating the tangent constitutive tensor previously defined in Eq. 14 the derivation of the damage variable with respect to the energetic norm, ψ, is

$$\frac{\partial G^j(\psi^j)}{\partial\psi^j} = -\frac{{\psi_0^j}^2}{{\psi^j}^2(1 + H^j)} \tag{17}$$

2.3 Finite–Element implementation

The proposed model is implemented within the commercial FE software Abaqus [44] through a coupled user material subroutine (UMAT). The algorithm is detailed in Appendix A. A 3D structural mesh made of hexahedral and/or wedge elements is reconstructed across the wall of the artery. The mesh is structural, which means that the edge of each element is locally aligned with the material directions of the artery; radial, circumferential and axial. For non–perfectly cylindrical geometries, the radial direction is defined as the outward normal direction to the luminal surface, the axial direction is defined as the direction parallel to the luminal centerline in the direction of the blood flow, and the circumferential direction is perpendicular to the two previously defined directions. It is assumed that each element is a mixture of elastin, collagen and SMCs with mass fractions varying regionally.
Collagen and SMCs are continuously produced and replaced during lifetime [55] while elastin is mainly stable after perinatal period for at least a few decades leading to large multiaxial stretches in the elastin constituent as the artery enlarges from infancy to adulthood [23, 55]. Deposition stretches of collagen fibers and SMCs can be experimentally characterized as explained previously [9, 34]. Therefore, deposition stretches of the SMCs constituent, G_h^{m}, and of the collagen constituents, $G_h^{\mathrm{c}_i}$, are set to $\sim$1.1 throughout the present work.
Assuming cylindrical coordinates, $\mathbf{G}_h^{\mathrm{e}} = \mathrm{diag}[\lambda_r \quad \lambda_\theta \quad \lambda_z^{iv}]$, where incompressibility reads $\lambda_r = \frac{1}{\lambda_\theta \lambda_z^{iv}}$, the axial deposition stretch of elastin, λ_z^{iv}, is assigned such as being able to induce the usual axial recoil that can be measured when the artery is excised (this axial stretch may depend on species, on the type of arteries, on the age, etc [48]). The circumferential component, λ_θ, is defined iteratively such that in the first step, it is set to one, $\lambda_\theta = 1$. Therefore, by applying diastolic pressure and taking into account deposition stretches of collagen and SMCs mentioned above, an FE analysis is performed for the first step. The deformation gradient of elastin, $\mathbf{F}^{\mathrm{e}}$, is recorded at the end of each step after convergence and assigned as the deposition stretch tensor of the elastin component in the next step until it converges to a stable value. The decision that deposition stretch tensor of the elastin is stable is made according to average nodal displacements across the arterial wall, U. So at the end of each step (at convergence of the algorithm), U must be less than a prescribed tolerance which is set to 1% of the wall thickness in the present work [63].

After calibrating the deposition stretch tensor of the elastin component the reference configuration including *in situ* residual stress is ready for FE analysis of the arterial wall to deduce damage initiation and evolution under different mechanical tests such as tensile, bulge inflation and patient specific simulations.

2.4 Collecting experimental data and fitting material parameters

Experimental protocol

An unruptured ATAA specimen was collected from patients undergoing elective surgery to replace their ATAA with a graft according to a protocol approved by the Institutional Review Board of the University Hospital Center of Saint-Etienne. The ATAA section was placed in saline solution and stored at 4°C from collection to testing. Tests were carried out within 48h after the surgery. A square of 45×45 mm was cut from the ATAA specimen and clamped in the bulge inflation device. The inflating region was a disc of diameter equal to 30mm. The luminal surface faced outward and then a speckle pattern was applied to the lumen by spraying graphite powder. To inflate the specimen, water was infused into the cavity behind the sample using a syringe pump driven at 2mL/min. During inflation of the sample, a digital manometer (WIKA, DG-10) was used to measure the pressure. Two 8-bit CCD cameras equipped with 50mm lenses (resolution: 1624×1236 px), positioned 50cm apart at an angle of 30° with an aperture of f/11, were used to collect images of the inflating specimen. A commercial Digital Image Correlation (DIC) system (GOM, 5M LT) was used to process the images by stereo Digital Image Correlation and obtain the 3D displacement fields across the surface of the samples. Therefore, the setup enabled us to produce a sufficient depth of field (15.4mm) to capture the deformation field of the tissue every 3kPa until the sample ruptured [24]. Curves of pressure versus peak deflection were plotted in Fig. 1 for two different patients.

Fitting material parameters

Mass fractions of the different constituents and deposition stretches of collagen fibers were taken from literature [8, 15]. The deposition stretches of elastin and its material parameter μ^e were calibrated in order to simulate

correctly the recoiling following excision and at the same time to ensure equilibrium between the prestress and the pressure at the reference configuration. The other parameters of the four-fiber family model reported in Table 1 (k_1^j and k_2^j, $j \in \{c_i, m\}$) were calibrated by adjusting the pressure–deflection curve predicted by the model against the experimental results. For that we calculated the sum of squares of the deviations between the measured deflection and the predicted deflection for all the pressures for which the displacement fields were measured. Then, for each measured deflection set of y_i with a predicted deflection set of f_i, we derived the coefficient of determination such as:

$$R^2 = 1 - \frac{\sum_{i=1}^{n}(y_i - f_i)^2}{\sum_{i=1}^{n}(y_i - \overline{y})^2} \tag{18}$$

where $\overline{y}$ represents the mean measured deflection data. Thus, R^2 quantifies the difference between modeling predictions and experimental data set. When R^2 is close to 1, the model predictions are very close to the experimental results. The cost function $1 - R^2$ was minimized using a genetic algorithm. At each iteration, the model resolution involved the complete procedure, including excision, flattening and bulge inflation to take into account the mechanical effects of excising and cutting starting from the in vivo tissue. Lower and upper bounds were defined for each parameter. The lower bound was used only to avoid null or negative values of parameters whereas the upper bound was set sufficiently high for not being reached. R^2 values reported in Table 1 indicate reasonably good fits to experimental data. The identification was performed for two sets of data corresponding to two different patients (Table 1). Fig. 1 shows both experimental and modeled pressure–deflection curves. A good agreement can be observed between the predictions of the numerical model and experimental data sets. Moreover, strain fields obtained with the CMT model were compared to the experimental strain fields deduced from DIC measurements at the maximum deflection during the bulge inflation test (Fig. 2). There is a good agreement between experimental strain fields and the model predictions, both for circumferential and axial components of the strain and for both patients, reflecting a successful identification of material parameters.

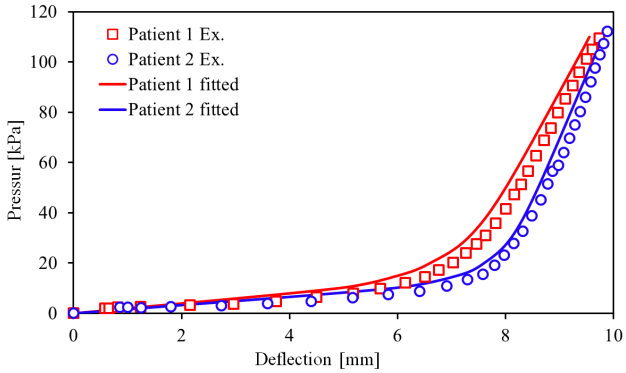

Figure 1: Pressure–deflection curve for bulge inflation tests of two patients. Solid lines demonstrate the fitted curve using material properties shown in Table 1.

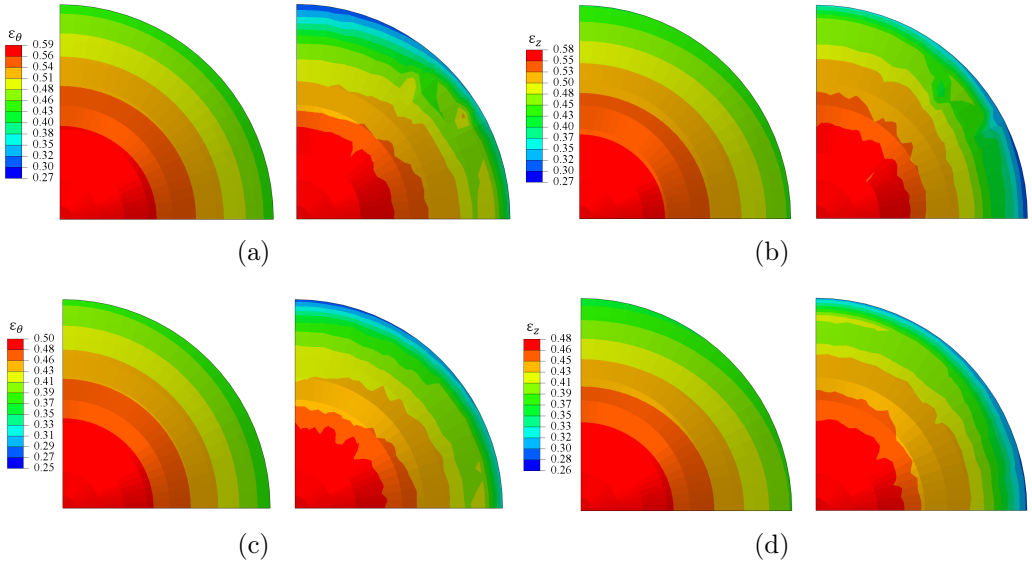

Figure 2: Top view of strain fields in circumferential and axial directions for patient 1 (a and b) and patient 2 (c and d) calculated by CMT model (left) and obtained from bulge inflation test (right).

Table 1: Material properties fitted to experimental data of bulge inflation tests for two different patients. Note that superscripts of c and t denote material properties under compression and tension, respectively. R^2 provides a quantitative measure of the quality of each fit.

Symbol	**Patient 1**	**Patient 2**
μ^{e}	82 [kPa]	71 [kPa]
$k_1^{\mathrm{c}_i,c} = k_1^{\mathrm{m},c}$	15 [kPa]	17 [kPa]
$k_2^{\mathrm{c}_i,c} = k_2^{\mathrm{m},c}$	1.0	1.0
$k_1^{\mathrm{c}_i,t}$	105 [kPa]	155 [kPa]
$k_2^{\mathrm{c}_i,t}$	0.13	0.16
$k_1^{\mathrm{m},t}$	10 [kPa]	10 [kPa]
$k_2^{\mathrm{m},t}$	0.1	0.1
ρ^{e}	0.25	0.25
ρ^{c_i}	0.46	0.46
ρ^{m}	0.28	0.28
R^2	0.983	0.988
	Damage parameters	
ψ_0^{e}	1.26 [kPa$^{1/2}$]	-
$\psi_0^{\mathrm{c}_i}$	3.09 [kPa$^{1/2}$]	-
$\Omega^{\mathrm{e}} = \Omega^{\mathrm{c}_i}$	45 [N/m]	-

2.5 Application to predict damage during inflation of a perfectly cylindrical artery

A thick–wall cylinder with outer diameter of 50 mm and thickness of 2.38 mm is meshed with 7500 hexahedral elements and with 10 elements across the thickness. At both ends of the cylinder only radial displacements are allowed while axial and circumferential displacements are blocked. Mass fractions ρ^{e}, ρ^{c_i} and ρ^{m} introduced in the expression of the SEF in Eq. 2 and material parameters are reported in Table 1. First the reference configuration is set arbitrarily as the one of the artery in the *in vivo* conditions of diastole. Afterwards, by increasing gradually luminal pressure, P_i, the FE analysis with the CMT–based damage model is employed to localize damage initiation and to calculate damage evolution across different layers of arterial wall. Using FE simulation, the initial damage threshold, ψ_0, is calculated based on the maximum pressure ($\sim$110 kPa will be explained in section 2.7) that the sample could bear under experimental bulge inflation test.

2.6 Application to predict damage during tensile test (uniaxial) of human ATAA strips

To simulate uniaxial tensile tests, in a first step, pressure and axial stretch of the thick–wall cylinder of the section 2.5 are set to zero and a radial cut is introduced to the arterial wall, allowing it to open and to flatten. The flattening is achieved by applying proper boundary conditions (namely displacement) to the cut edge surface of the cylinder. This permits to preserve assigned *in vivo* deposition stretches of each constituent during tensile test. In the second step, appropriate displacement is applied on the cut edge to uniaxially load the flatten strip in the circumferential direction.

2.7 Application to predict the damage evolution of the arterial wall during bulge inflation tests

Another application of the model can be to simulate bulge inflation tests on a flatten sample of artery. As mentioned previously in section 2.4, taking into account the mechanical effects of excising and cutting the sample from the *in vivo* tissue. Here again the reference configuration is set arbitrarily as the one of the artery in the *in vivo* conditions of diastole, before modeling

the bulge inflation test. Thus, initially a segment of artery is pressurized and axially stretched to find the circumferential component of deposition stretch of elastin in the reference configuration. Afterwards, the average deformation gradient of each layer of the mixture is calculated during the flattening step of the tissue, namely $\mathbf{F}_f^k$, $k = 1, 2, ..., m$ with m number of layers. To simulate bulge the inflation test, a disc of 30 mm diameter and with the same thickness and number of layers as the arterial segment is meshed using wedge and hexahedral elements. The disc is pressurized keeping the primary deposition stretches of each constituent in reference configuration and applying $\mathbf{F}_f^k$ onto the corresponding layer of the disc.

2.8 Application to predict damage evolution during overpressure in a patient specific ATAA

The FE model is finally applied onto a patient–specific geometry to demonstrate its capability for predicting damage evolution in a human ascending thoracic aortic aneurysm (ATAA). An ATAA specimen and the preoperative CT scan of the patient is obtained after informed consent from a donor undergoing elective surgery for ATAA repair at CHU-SE (Saint-Etienne, France). The lumen of the aneurysm is clearly visible in the DICOM file, but the aneurysm surface is not automatically detectable. The digital caliper is used to homogeneously measure the thickness of the excised aneurysm *in vitro* [77, 78]. A 2.5 mm average wall thickness is measured on the supplied sample corresponding to the zero pressure configuration. A non-automatic segmentation of the CT image slices is performed using MIMICS (v. 10.01, Materialise NV) to reconstruct the ATAA geometry and export it as a STL file. VMTK [2] was employed to generate the structural mesh for a membrane obtained from the STL file. The extracted data from VMTK is postprocessed in Matlab to extract an accurate structural mesh using the longitudinal and circumferential metrics obtained from VMTK. The mesh morphing function is then interpolated at every node of the template mesh using a least-squares method. Finally, using the thickness measured in the reference configuration, the membrane structural mesh is duplicated in eleven layers to generate ten layers of hexahedral elements across the thickness where each layer of media and adventitia has five. The material parameters are the ones of the first patient in Table 1. The reference configuration is defined with a luminal pressure of 80 mmHg which corresponds to the diastolic pressure. An axial

prestretch (deposition stretch) of $\lambda_z^{\text{iv}} = 1.3$ is defined for the elastin component and the deposition stretches of collagen and SMC components are set to 1.1. The circumferential deposition stretch of elastin is determined iteratively as explained in section 2.3 [63]. Afterwards, damage evolution in the ATAA wall is analyzed using the CMT–based damage model by increasing gradually the luminal pressure. As boundary conditions, at both ends of the ATAA model, only radial displacements are allowed and displacements in the circumferential and axial direction are blocked.

3 Results

3.1 Damage evolution during inflation of a perfect thick-wall cylinder

The distribution of damage evolution is shown as a colormap in Fig. 3. It illustrates that damage always starts on the luminal side at the innermost position in the media layer. The damaged component of the model is elastin as the initial damage threshold of collagen in the model was higher than that of elastin. Here, damage starts at $P_i \simeq 28.5$ kPa and increasing the luminal pressure causes damage to propagate outwards radially in the media and finally to spread across the whole media. The maximum applicable luminal pressure in this case is $P_i \simeq 30.1$ kPa and due to extensive softening of the media in consequence of damage, further pressurizing of the cylinder is not possible. Accordingly damage stays in the elastin constituent in the media and does not propagate to the adventitia.

3.2 Damage evolution during tensile test (uniaxial) of human ATAA strips

Figs. 4-a and 4-b show damage evolution of a human ATAA strip under uniaxial tensile loading after its opening and flattening by introducing a radial cut. Damage evolution in Figs. 4-a is obtained with the CMT model and damage evolution in Figs. 4-b is obtained with a traditional model without prestrain. It can be seen that both models always predict damage initiation on the luminal side at the innermost position in the media layer and again, only the elastin constituent is concerned by damage. This is consistent with the experimental results obtained in our group (unpublished) indicating that

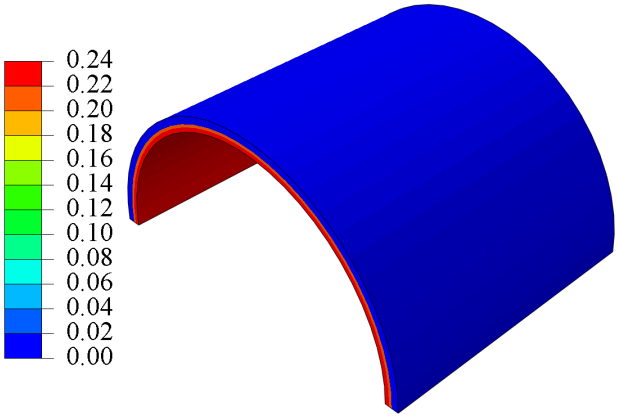

Figure 3: Damage evolution during inflation of a perfect thick-wall cylinder.

uniaxial stretching of the arterial tissue leads to a progressive delamination of the tissue, layer by layer, starting from the luminal side. Besides, it is experimentally shown that media has a significantly smaller strength in the axial direction when subjected to uniaxial tension [76]. Further stretching of the strip leads to the outwards radial propagation of damage in the media layer but it remains in the elastin constituent due to the higher initial damage threshold of collagen fibers. However, for the same stretch applied to the ATAA strip, smaller damage variables are obtained with the CMT model. For both cases again, damage does not propagate into the adventitia, this time due to divergence of the resolution. Transmural distribution of the in-plane and through-the-thickness stresses at the onset of damage initiation is plotted in Fig. 5 for the CMT model. As expected, there is a discontinuity of stresses at the interface between the media and the adventitia for each case, due to discontinuous material properties. Through-the-thickness stresses are two orders of magnitude smaller than in-plane stresses and consequently, as an isotropic damage model was considered for elastin, damage was triggered by in-plane stresses and not through-the-thickness stresses.

3.3 Damage evolution of the arterial wall during bulge inflation tests

The distribution of damage evolution for a bulge inflation test is shown in Fig. 6 for two situations:

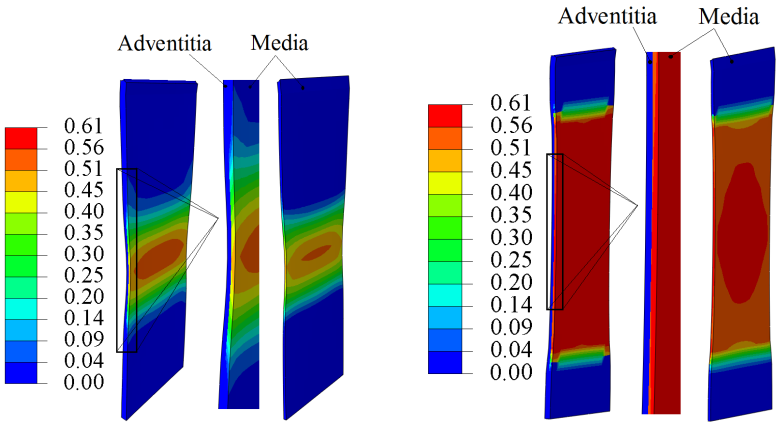

(a) (b)

Figure 4: Damage evolution of a human ATAA strip under uniaxial tension after its opening and flattening by introducing a radial cut. a- using CMT model, b- using traditional model (without prestrain).

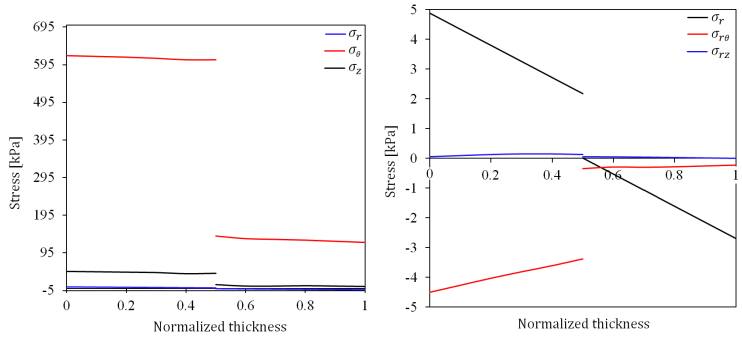

(a) (b)

Figure 5: Transmural distribution of normal Cauchy stresses through the thickness in radial, circumferential and axial directions (a) and radial shear stresses (b) during uniaxial tensile test predicted using CMT model at the onset of of damage initiation. All stress components are plotted as function of the normalized thickness, with 0 and 1 corresponding to the inner and outer surface of the artery,, respectively.

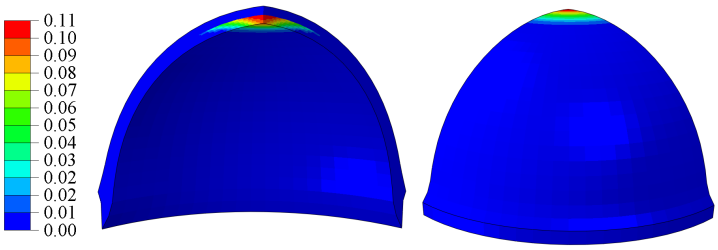

(a)

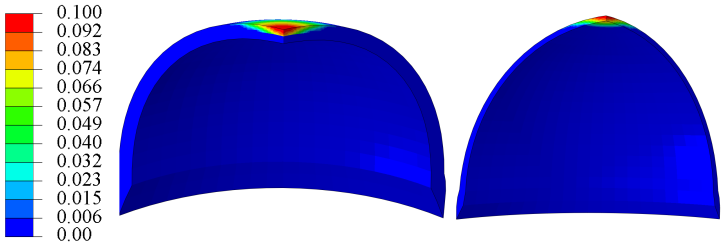

(b)

Figure 6: Damage evolution during bulge inflation of a human ATAA. a- The situation with the luminal side of the aorta inside, b- The situation with the luminal side of the aorta outside. In the left, both layers together are shown while in the right one just media is shown.

1. the first situation is with the luminal side of the aorta inside (Fig. 6-a). In this case, damage always starts at the boundary between the media and the adventitia and then propagates radially inwards across the media thickness. Softening of the media due to damage evolution permits to pressurize the sample up to $P_i \simeq 114$ kPa. After propagation across the whole media, the pressure drops and the resolution diverges.

2. the second situation is with the luminal side of the aorta outside so that the aorta is mounted upside down in the device (Fig. 6-b). Experimentally this situation was used to permit painting the surface and track the deformation during the test with DIC [25, 24, 30, 73]. Indeed, the luminal surface is smoother and cleaner, permitting a better optical contrast. In this situation with the luminal side of the aorta outside, damage initiates on the outermost surface of the sample (luminal side) and propagates radially across the media.

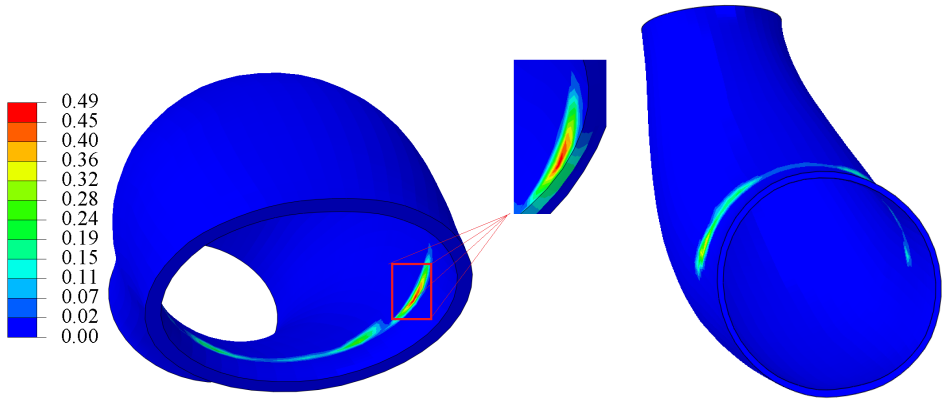

(a) (b)

Figure 7: Damage evolution during inflation of patient specific geometry. a- Both layers together, b- media.

3.4 Damage evolution during over-pressurizing of a patient-specific ATAA

Damage distributions for a patient-specific ATAA geometry subjected to over-pressurizing is shown in Fig. 7. The parameters of the model used for these simulations, including ψ_0, came from the model calibration against the experimental data of the bulge inflation test carried out on the aortic segment of the same patient. Focusing on the location with maximum damage it is observed that damage initiates on the luminal side and propagates across the media layer. Interestingly, damage mostly occurs in the inner curvature of the aneurysm. This is a clear demonstration of the transition between homogeneous damage (which occurred in the cylinder problem of Section 3.1) and the situation in which damage is localized into small regions that would manifest physically as a crack (see our experimental results of ATAA rupture in [30, 73]). Damage starts at $P_i \simeq 35.2$ kPa which is more than 2.5 times a normal blood pressure (13 kPa) and the geometry can be inflated up to $P_i \simeq 45.8$ kPa. Before damage affects the adventitia, softening of the media prevents further inflation of the ATAA due to resolution divergence. The results indicate though that, due to damage evolution, an ATAA may be prone to undergo dissection by media rupture not followed by an adventitia rupture, but most probably by a crack propagation at the interface between the two layers (not simulated here).

4 Discussion

The important potential of the constrained mixture theory (CMT) has already shown for predicting the mechanobiological behaviour of arteries based on anisotropic hyperelastic models [8, 15, 50, 53, 63, 79]. In the present paper, we combined for the first time the CMT approach with a damage model for predicting layer-specific damage initiation in arteries during over-pressure loading. The constitutive parameters of the novel model were calibrated against experimental data before simulating damage initiation in different situations, including patient-specific ATAA. As FE analyses are extensively employed for soft tissue damage, it is important to take into account the *in vivo* stress distribution of the tissue which may correspond to clinical situations [26]. The CMT approach presents the advantage of including the actual *in vivo* state of stress of each constituent in a layer-specific fashion. Therefore, the present numerical framework can be considered as a clinically relevant tool.

As discussed in [63], different material parameters for the media and adventitia render discontinuous circumferential and axial stresses at the interface between the media and adventitia, supported also by [8, 46, 82]. In addition to the different material parameters, it is required to introduce two deposition stretches for the elastin, one axial and one circumferential which are calibrated in order to ensure: (i) that the stresses in the wall of the artery balance the luminal pressure present in the reference in vivo diastolic configuration. (ii) that the axial recoil of the artery upon excision is predicted correctly. We first assign a constant axial deposition stretch at all Gauss points (the value is calibrated to ensure that the axial recoil of the artery upon excision is predicted correctly). Then we run the iterative finite element analysis to calibrate the circumferential deposition stretch at every Gauss point. During the iterations we do not modify the axial deposition stretch. Satisfying condition (i) may induce a sensitivity of the calibrated circumferential deposition stretch of the elastin with respect to the elastin material parameter μ^{e}. In order to use the correct value of parameter μ^{e}, we have to simulate an excision after running the iterative algorithm and reconstructing the distribution of circumferential deposition stretch. Then the average radial recoil during the simulated excision has to be compared to the actual radial recoil and parameter μ^{e} must be updated. Then the iterative algorithm has to be run again to find another distribution of circumferential deposition stretch that permits satisfying equilibrium. The loop is repeated

until the choice of parameter μ^{e} and the deduced deposition stretches yield the correct actual recoil when the excision is simulated. Only the simulation of arterial excision can validate the choice of deposition stretch for the elastin.

Parameters of our four–fiber family model were calibrated by adjusting the pressure–deflection curves against the experimental results. Abundant literature can be found about the resolution of similar identification problems where authors have investigated the unicity of the solution [3, 4, 35]. The question of unicity arises especially for bi-layer models, as discussed by Badel et al [5]. The identification of the fiber angle parameter in two–fiber family models [36] particularly needs to satisfy constraints for ensuring a unique solution to the problem [47]. For instance, bounds can be defined to ensure that fibers remain closer to the axial direction in the adventitia and closer to the circumferential direction in the media. In our case, as we used a four-fiber family model, we assumed a similar angle for diagonal fibers in the media and in the adventitia, but we assigned different mass fractions of each type of fibers (circumferential, axial and diagonal) between two layers. Other authors like Qi et al. [69] employed the κ-model [40] extended from the Holzapfel model [46] to model fiber orientations. They suggested that if upper and lower bounds are properly chosen, the parameters can be identified uniquely. Another important aspect of the identification is the minimization algorithm. The standard nonlinear Levenberg–Marquardt algorithm [47, 62, 69] is commonly used for the identification of material parameters such as Neo–Hookean, exponential coefficients or fiber angles. In the current work we used a genetic algorithm which ensures a global minimum. It was shown to be less sensitive to the mutual influence between k_1^j and k_2^j coefficients of exponential strain energy density functions [10].

One of the specificity of the current approach is that the reference configuration is set arbitrarily to the *in vivo* diastolic configuration. In this configuration, the diastolic pressure applied onto the artery is balanced by tissue prestress. A different prestress is assigned to each constituent by assigning a so-called deposition stretch. Whilst the deposition stretch of collagen was previously estimated experimentally [34], the deposition stretch of elastin is calibrated iteratively before each simulation in order to find the values that will provide mechanical equilibrium [63]. At the end of the iterative approach, there should be a displacement of less than 1% of the arterial thickness to the application of the diastolic pressure, ensuring a perfect equilibrium. However, it was numerically difficult to reach this 1% threshold at specific positions of

patient specific ATAA geometries. It was due to highly curved configuration which lead to significant local stress gradients, with through-thickness shear stresses especially between media and adventitia. At these locations, we still had a displacement of about 10% of the arterial thickness after calibrating the elastin deposition stretch. However, these locations were not concerned by damage initiation and consequently this did not have an impact on the results.

The most relevant results in simulations of damage initiation is the prediction of damage propagation across the aortic wall, starting from the intimal layer (luminal side) and propagating across the whole media, but not hitting the adventitia. This means that, at high blood pressure, a partial rupture of the arterial thickness can be predicted. This can be related clinically to acute dissection development. Despite of large advances in diagnosis and surgery of ATAA, acute dissection remain the most common crucial complication of an ATAA, with significant mortality [13]. Dissection commonly occurs in elderly patients having a tricuspid aortic valve and can also hit relatively young patients having a bicuspid aortic valve [14]. We suggest that conditions such as aging or bicuspid aortic valve, which are known to affect the biochemistry of the wall [11] and consequently reduce through-thickness radial strength of the aorta, would be favorable for deviating a crack propagating radialy across the whole media. Crack deviation means that the crack would kink and propagate tangentially between the media and the adventitia. Our results presented here reveal that the media is prone to undergo such rupture when the arterial wall is overloaded, but we did not simulate the crack deviation, we just showed that the crack propagation was stopped when it reached the adventitia. Crack deviation and further delamination could possibly be modelled using cohesive zone elements [6, 59], but this was out of scope here. Nevertheless, this scenario of dissection initiation was observed in most of the bulge inflation tests carried out on aortic samples when the sample was mounted with the luminal side out, similar to the numerical prediction [30]. Interestingly when the bulge inflation test was carried out with samples mounted with the luminal side in, we observed strain localization but not a dissection-like rupture [73]. This is also predicted by the model which shows that, in such situation, damage will initiate in the inter–layer position and propagate radially inwards, without reaching the outside position. The scenario of dissection initiation, starting with a partial rupture of the arterial thickness, is also confirmed by tensile tests performed on completely delaminated ATAA samples by Pasta et al. [66]. They demonstrated that

the intima-media half of the aortic wall may undergo failure before the outer adventitial half. Tear initiation in ascending aortic dissection was shown to occur in the region close to the sinotubular junction which experiences the maximum wall stresses [20]. This tear is highly hazardous, even often lethal, as it permits blood to enter the aortic wall and consequently split progressively the media and separate it along the axial direction of the aorta.

4.1 Study limitations

Despite the interesting observations made with the current model, several limitations should be listed.

The viscoelastic effect is ignored in this work. Although some authors suggested it was not significant in damage of anisotropic soft tissue [18, 52], we plan to consider viscoelastic effects in future studies to verify this assumption.

Moreover, in this work fiber–fiber and fiber–matrix interactions are neglected. Such interactions may become important for the time–dependent response. Therefore, a plasticity theory could be appropriate, as the nonlinear behaviour of collagen fibers may cause irresversible slips of fibers one over another.

The material parameters, including mass fractions and deposition stretches of each constituent, were estimated by calibrating the model against the response to bulge inflation. There is a pressing need to develop a non-invasive methodology to obtain *in vivo* material parameters which would be relevant for clinical applications.

In the present work, for patient-specific analyses of human ATAAs, the wall thickness is assumed homogeneous. However it is shown by some authors [16] that thickness varies in an ascending thoracic aorta. Although this can be considered as a limitation of this work, it is possible to include these variations in the present model if data are available. Nevertheless, it is also shown that these thickness variations are less important in aneurysms than in healthy aortas [16]. The effect of possible regional variations in the thickness and in the material properties, would obviously affect the local values of deposition stretches that we have to assign to elastin, as shown in another paper where the regional variations of a CMT-based model were reconstructed on mice aortas [10].

There is no clinical evidence that a dissection would actually appear on the inner curvature of the aortic arch. Most dissection would even occur

on the outer curvature side [66]. However, in our model, we used the same damage initiation threshold and same material properties everywhere. In reality, material properties may vary regionally [51, 67, 86]. So it may happen that even if the maximum stress is at the inner curvature side, the location where the damage threshold is reached first may be on the outer curvature side in reality, because this side may be weaker. This reveals the importance of taking into account the regional variations of material properties in the models.

In this model we have assumed an isotropic damage criterion. As noted above, through-the-thickness stresses are smaller than in-plane stresses and consequently, as we have an isotropic damage model for elastin, damage initiates in the plane and not through-the-thickness. Therefore it would be very interesting to introduce an anisotropic damage criterion and investigate how in-plane and through-the-thickness damage can interplay in that case.

5 Conclusions

In summary, in the present work, a novel layer–specific damage model based on the constrained mixture theory (CMT) was presented, it was implemented robustly in a finite-element framework and its applicability was demonstrated by different examples such as uniaxial tensile tests, bulge inflation tests and patient-specific over–pressurization of a human aortic aneurysm. The main advantage of the present model is that the numerical framework is flexible and material definition can be conveniently augmented with new components such as growth and remodeling in the strain energy function and in the damage formulation. We are currently following this direction for predicting patient-specific damage evolution and possible risk of dissection during aneurysm growth.

6 Conflict of interest

There is no conflict of interest.

7 Acknowledgements

The authors are grateful to the European Research Council for grant ERC-2014-CoG BIOLOCHANICS.

Appendix A Algorithm of the numerical implementation of the model at Gauss point level

Initialization at $t = 0$ and $n = 0$

set $D^{j\,n+1} = D^{j\,n} = 0, j \in \{\mathrm{e}, \mathrm{c}_i\}$

At each time increment n+1

For corresponding mixture deformation gradient, $\mathbf{F}$, calculate $\overline{I}_1^{\mathrm{e}}$, $I_4^{\mathrm{c}_i}$ and I_4^{m}.

Compute the second Piola-Kirchhoff stress tensor, $\mathbf{S}$, using Eq. 12 and the

corresponding tangent constitutive tensor, $\mathbb{C}$, using Eq. 14.

Calculate the undamaged deviatoric part of the Helmholtz free energy for

elastin, $\overline{W}^{\mathrm{e}}$, and collagen families, $\overline{W}^{\mathrm{c}_i}$, from Eqs. 3 and 6, respectively, and

determine the present damage threshold of each constituent, ψ^{e} and ψ^{c_i}, from

Eq. 16.

if $\psi^j > \psi_0^j, j \in \{\mathrm{e}, \mathrm{c}_i\}$ (damage progresses) **then**

Compute the mechanical damage for the current increment, $D^{j\,n+1}$, and $\frac{\partial G^j(\psi^j)}{\partial \psi^j}$ using Eqs. 16 and 17, respectively.

if $D^{j\,n+1} < D^{j\,n}$ (elastic unloading) **then**

$\frac{\partial G^j(\psi^j)}{\partial \psi^j} = 0$

end if

else

$D^{j\,n+1} = D^{j\,n}$

$\frac{\partial G^j(\psi^j)}{\partial \psi^j} = 0$

end if

Using current damage, $D^{j\,n+1}$, update the second Piola-Kirchhoff stress tensor, $\mathbf{S}$, using Eq. 12 and the corresponding tangent constitutive tensor,

$\mathbb{C}$, using Eq. 14.

References

[1] V. Alastrué, J.F. Rodríguez, B. Calvo, and M. Doblaré. Structural damage models for fibrous biological soft tissues. *Int J Solids Struct*, 44:5894–911, 2007.

[2] L. Antiga and D.A. Steinman. Robust and objective decomposition and mapping of bifurcating vessels. *IEEE Trans Med Imaging*, 23(6):704–13, 2004 Jun.

[3] S. Avril. *Hyperelasticity of Soft Tissues and Related Inverse Problems. In Material Parameter Identification and Inverse Problems in Soft Tissue Biomechanics*, volume 573. Springer International Publishing, 2017.

[4] S. Avril, P. Badel, M. Gabr, M.A. Sutton, and S.M. Lessner. Biomechanics of porcine renal arteries and role of axial stretch. *J Biomech Eng*, 135(8):081007, 2013.

[5] P. Badel, S. Avril, S. Lessner, and M. Sutton. Mechanical identification of layer-specific properties of mouse carotid arteries using 3D-DIC and a hyperelastic anisotropic constitutive model. *Comput Methods Biomech Biomed Engin*, 2012:37–48, 15(1).

[6] P. Badel, S. Avril, M.A. Sutton, and S.M. Lessner. Numerical simulation of arterial dissection during balloon angioplasty of atherosclerotic coronary arteries. *J Biomech*, 47(4):878–89, 2014.

[7] D. Balzani, S. Brinkhues, and G.A. Holzapfel. Constitutive framework for the modeling of damage in collagenous soft tissues with application to arterial walls. *Comput Methods Biomech Biomed Engin*, 213–16,:139–51, 2012.

[8] C. Bellini, J. Ferruzzi, S. Roccabianca, E.S. Di Martino, and J.D. Humphrey. A microstructurally motivated model of arterial wall mechanics with mechanobiological implications. *Ann Biomed Eng*, 42(3):488–502, 2014.

[9] C. Bellini, N.J. Kristofik, M.R. Bersi, T.R. Kyriakides, and J.D. Humphrey. A hidden structural vulnerability in the thrombospondin-2 deficient aorta increases the propensity to intramural delamination. *J Mech Behav Biomed Mater*, 71:397–406, 2017.

[10] M.R. Bersi, C. Bellini, P. Di Achille, J.D. Humphrey, K. Genovese, and S. Avril. Novel methodology for characterizing regional variations in the material properties of murine. *J Biomech Eng*, 138(7):doi: 10.1115/1.4033674, 2016.

[11] M. Billaud, J.A. Phillippi, M.P. Kotlarczyk, J.C. Hill, B.W. Ellis, C.M. St Croix, N. Cantu-MedÃľllin, E.E. Kelley, and T.G. leason. Elevated oxidative stress in the aortic media of patients with bicuspid aortic valve. *J Thorac Cardiovasc Surg*, page doi: 10.1016/j.jtcvs.2017.05.065, 2017.

[12] S. Blanco, C.A. Polindara, and J.M. Goicolea. A regularised continuum damage model based on the mesoscopic scale for soft tissue. *Int J Solids Struct*, 58:20–33, 2015.

[13] C.R. Bonnichsen, T.M. Sundt 3rd, N.S. Anavekar, T.A. Foley, M.F. Morris, M.W. Martinez, E.E. Williamson, J.F. Glockner, and P.A. Araoz. Aneurysms of the ascending aorta and arch: the role of imaging in diagnosis and surgical management. *Expert Rev Cardiovasc Ther*, 9(1):45–61, 2011.

[14] J.M. Burks, R.W. Illes, E.C. Keating, and W.J. Lubbe. Ascending aortic aneurysm and dissection in young adults with bicuspid aortic valve: implications for echocardiographic surveillance. *Clin Cardiol*, 21(6):439–43, 1998.

[15] L. Cardamone, A. Valentin, J.F. Eberth, and J.D. Humphrey. Origin of axial prestretch and residual stress in arteries. *Biomech Model Mechanobiol*, 8(6):431–46, 2009.

[16] N. Choudhury, O. Bouchot, L. Rouleau, D. Tremblay, R. Cartier, J. Butany, R. Mongrain, and R.L. Leask. Local mechanical and structural properties of healthy and diseased human ascending aorta tissue. *Cardiovasc Pathol*, 18(2):83–91, 2009.

[17] B.M. Chu and P.J. Blatz. Cumulative microdamage model to describe the hysteresis of living tissue. *Ann Biomed Eng*, 1(2):204–11, 1972.

[18] C. Chui, E. Kobayashi, X. Chen, T. Hisada, and I. Sakuma. Transversely isotropic properties of porcine liver tissue: Experiments and constitutive modeling. *Med Bio Eng Comput*, 45:99–106, 2007.

[19] C.J. Chuong and Y.C. Fung. On residual stresses in arteries. *J Biomech*, 108(2):189–92, 1986.

[20] M.A. Coady, J.A. Rizzo, L.J. Goldstein, and J.A. Elefteriades. Natural history, pathogenesis, and etiology of thoracic aortic aneurysms and dissections. *Cardiol Clin*, 17(4):615–35, 1999.

[21] E. Comellas, F. Bellomo, and S. Oller. A generalized finite-strain damage model for quasi-incompressible hyperelasticity using hybrid formulation. *Comput Methods Biomech Biomed Engin*, 105(10):781–800, 2016.

[22] E. Comellas, T.C. Gasser, F.J. Bellomo, and S. Oller. A homeostatic-driven turnover remodelling constitutive model for healing in soft tissues. *J R Soc Interface*, 13(116):20151081, 2016.

[23] E.C. Davis. Elastic lamina growth in the developing mouse aorta. *J Histochem Cytochem*, 43(11):1115–23, 1995.

[24] F.M. Davis, Y. Luo, S. Avril, A. Duprey, and J. Lu. Pointwise characterization of the elastic properties of planar soft tissues: application to ascending thoracic aneurysms. *Biomech Model Mechanobiol*, 14(5):967–78, 2015(5).

[25] F.M. Davis, Y. Luo, S. Avril, A. Duprey, and J. Lu. Local mechanical properties of human ascending thoracic aneurysms. *J Mech Behav Biomed Mater*, 61:235–49, 2016.

[26] S. De, J. Rosen, A. Dagan, B. Hannaford, P. Swanson, and M. Sinanan. Assessment of tissue damage due to mechanical stresses. *Int J Rob Res*, 26:1159–71, 2007.

[27] M. Doblaré and J.M. García. Anisotropic bone remodelling model based on a continuum damage-repair theory. *J Biomech*, 35(1):1–17, 2002.

[28] K.L. Dorrington and N.G. McCrum. Elastin as rubber. *Biopolymers*, 16(6):1201–22, 1977.

[29] A. Duprey, K. Khanafer, M. Schlicht, S. Avril, D. Williams, and R. Berguer. In vitro characterisation of physiological and maximum elastic modulus of ascending thoracic aortic aneurysms using uniaxial tensile testing. *Eur J Vasc Endovasc Surg*, 39(6):700–7, 2010.

[30] A. Duprey, O. Trabels, M. Vola, J.P. Favre, and S. Avril. Biaxial rupture properties of ascending thoracic aortic aneurysms. *Acta Biomater*, 42:273–85, 2016.

[31] F.J. Bellomo E. Comellas and and S.Oller. A generalized finite-strain damage model for quasi-incompressible hyperelasticity using hybrid formulation. *Int J Numer Method Biomed Eng*, doi:10.1002/nme.5118, 2015.

[32] S. Farzaneh, O. Paseta, and M.J. Gómez-Benito. Multi-scale finite element model of growth plate damage during the development of slipped capital femoral epiphysis. *Biomech Model Mechanobiol*, 14(2):371–85, 2015.

[33] J.P.S. Ferreira, M.P.L. Parente, M. Jabareen, and R.M. Natal Jorge. A general framework for the numerical implementation of anisotropic hyperelastic material models including non-local damage. *Biomech Model Mechanobiol*, 16(4):1119–40, 2017.

[34] J. Ferruzzi, M.J. Collins, A.T. Yeh, and J.D. Humphrey. Mechanical assessment of elastin integrity in fibrillin-1-deficient carotid arteries: implications for Marfan syndrome. *Cardiovasc Res*, 92(2):287–9, 2011.

[35] J. Ferruzzi, D.A. Vorp, and J.D. Humphrey. On constitutive descriptors of the biaxial mechanical behaviour of human abdominal aorta and aneurysms. *J R Soc Interface*, 8(56):435–50, 2010.

[36] H.M. Finlay, L. McCullough, and P.B. Canham. Three-dimensional collagen organization of human brain arteries at different transmural pressures. *J Vasc Res*, 32(5):301–12, 1995.

[37] YC. Fung. What principle governs the stress distribution in living organism? *Biomechanics in China, Japan, and USA. Proc. of Wuhan Conf., Science Press, Beijing, China, May*, 1983.

[38] C.M. García-Herrera, D.J. Celentano, M.A. Cruchaga, F.J. Rojo, J.M. Atienza, G.V. Guinea, and J.M. Goicolea. Mechanical characterisation of the human thoracic descending aorta: experiments and modelling. *Comput Methods Biomech Biomed Engin*, 15(2):185–93, 2012.

[39] T.C. Gasser. An irreversible constitutive model for fibrous soft biological tissue: A 3-D microfiber approach with demonstrative application to abdominal aortic aneurysms. *Acta Biomater*, 7(6):2457–66, 2011.

[40] T.C. Gasser, R.W. Ogden, and G.A. Holzapfel. Hyperelastic modelling of arterial layers with distributed collagen fibre orientations. *J R Soc Interface*, 3(6):15–35, 2006.

[41] M.J. Gómez-Benito, P. Moreo, M.A. Pérez, O. Paseta, J.M. García-Aznar, C. Barrios, and M. Doblaré. A damage model for the growth plate: Application to the prediction of slipped capital epiphysis. *J Biomech*, 40(15):3305–13, 2007.

[42] J.M. Guccione, A.D. McCulloch, and L.K. Waldman. Passive material properties of intact ventricular myocardium determined from a cylindrical model. *J Biomech Eng*, 113(1):42–55, 1991.

[43] Z. Guo and R. De Vita. Probabilistic constitutive law for damage in ligaments. *Med Eng Phys*, 31(9):1104–09, 2009.

[44] Hibbit, Karlson, and Sorensen. *Abaqus-Theory manual*, 6.11-3 edition, 2011.

[45] G.A. Holzapfel. *Nonlinear Solid Mechanics. A Continuum Approach for Engineering*. Wiley, Chichester, 2000.

[46] G.A. Holzapfel, T.C. Gasser, and R.W. Ogden. A new constitutive framework for arterial wall mechanics and a comparative study of material models. *J. Elast.*, 61:1–48, 2000.

[47] G.A. Holzapfel, T.C. Gasser, and R.W. Ogden. Comparison of a multilayer structural model for arterial walls with a fung-type model, and issues of material stability. *J Biomech Eng*, 126(2):264–75, 2004.

[48] L. Horný, M. Netušil, and T. Voňavková. Axial prestretch and circumferential distensibility in biomechanics of abdominal aorta. *Biomech Model Mechanobiol*, 13(4):783–99, 2014.

[49] J.D. Humphrey. *Cardiovascular Solid Mechanics: Cells, Tissues, and Organs*. Springer-Verlag NY, 2002.

[50] J.D. Humphrey and K.R. Rajagopal. A constrained mixture model for growth and remodeling of soft tissues. *Math Models Methods Appl Sci*, 12(3):407–430, 2002.

[51] D.C. Iliopoulos, R.P. Deveja, E.P. Kritharis, D. Perrea, G.D. Sionis, K. Toutouzas, C. Stefanadis, and D.P. Sokolis. Regional and directional variations in the mechanical properties of ascending thoracic aortic aneurysms. *Med Eng Phys*, 31(1):1–9, 2009.

[52] M. Kaliske, L. Nasdala, and H. Rothert. On damage modelling for elastic and viscoelastic materials at large strain. *Comput Struct*, 79(22–25):2133–41, 2001.

[53] I. Karsaj, J. Soric, and J.D. Humphrey. A 3-D framework for arterial growth and remodeling in response to altered hemodynamics. *Int J Eng Sci*, 48(11):1357–72, 2010.

[54] J.H. Kim, S. Avril, A. Duprey, and J.P. Favre. Experimental characterization of rupture in human aortic aneurysms using a full-field measurement technique. *Biomech Model Mechanobiol*, 11(6):841–53, 2012.

[55] B.L. Langille. Arterial remodeling: relation to hemodynamics. *Can J Physiol Pharmacol*, 74(7):834–41, 1996.

[56] D. Li and A.M. Robertson. A structural multi-mechanism damage model for cerebral arterial tissue. *J Biomech Eng*, 131(10):101013, 2009.

[57] S.A. Maas, A. Erdemir, J.P. Halloran, and J.A. Weiss. A general framework for application of prestrain to computational models of biological materials. *J. Mech Behav Biomed Mater*, 61:499–510, 2016.

[58] S.P. Marra, F.E. Kennedy, J.N. Kinkaid, and M.F. Fillinger. Elastic and rupture properties of porcine aortic tissue measured using in ation testing. *Cardiovasc Eng*, 6(4):123–31, 2006.

[59] B. Merei, P. Badel, L. Davis, M.A. Sutton, S. Avril, and S.M. Lessner. Atherosclerotic plaque delamination: Experiments and 2D finite element model to simulate plaque peeling in two strains of transgenic mice. *J Mech Behav Biomed Mater*, 67:19–30, 2017.

[60] D. Mohan and J.W. Melvin. Failure properties of passive human aortic tissue. I-uniaxial tension test. *J Biomech*, 15:887–902, 1982.

[61] D. Mohan and J.W. Melvin. Failure properties of passive human aortic tissue. II-biaxial tension test. *J Biomech*, 16(1):31–44, 1983.

[62] J.J. Moré. The levenberg-marquardt algorithm: implementation and theory. *Numer Anal*, 630:105–16, 1978.

[63] S.J. Mousavi and S. Avril. Patient-specific stress analyses in the ascending thoracic aorta using a finite-element implementation of the constrained-mixture theory. *Biomech Model Mechanobiol*, 16(5):1765–77, 2017.

[64] J. Oliver. A consistent characteristic length for smeared cracking models. *Int J Numer Method Biomed Eng*, 28(2):461–74, 1989.

[65] J.H. Omens and Y.C. Fung. Residual strain in rat left ventricle. *Circ Res*, 66(1):37–45, 1990.

[66] S. Pasta, J.A. Phillippi, T.G. Gleason, and D.A. Vorp. Effect of aneurysm on the mechanical dissection properties of the human ascending thoracic aorta. *J Thorac Cardiovasc Surg*, 143(2):460–7, 2012.

[67] S. Pasta, A. Rinaudo, A. Luca, M. Pilato, C. Scardulla, T.G. Gleason, and D.A. Vorp. Difference in hemodynamic and wall stress of ascending thoracic aortic aneurysms with bicuspid and tricuspid aortic valve. *J Biomech*, 46(10):1729–38, 2013.

[68] E. Peña. Damage functions of the internal variables for soft biological fibred tissues. *Mech Res Commun*, 38(8):610–15, 2011.

[69] N. Qi, H. Gao H, R.W. Ogden, N.A. Hill, G.A. Holzapfel, H.C. Han, and X. Luo. Investigation of the optimal collagen fibre orientation in human iliac arteries. *J Mech Behav Biomed Mater*, 52:108–19, 2015.

[70] M.K. Rausch and E. Kuhl. On the effect of prestrain and residual stress in thin biological membranes. *J Mech Phys*, 61(9):1955–69, 2013.

[71] F. Riveros, S. Chandra, E.A. Finol, T.C. Gasser, and J.F. Rodriguez. A pull-back algorithm to determine the unloaded vascular geometry in anisotropic hyperelastic aaa passive mechanics. *Ann Biomed Eng*, 41(4):694–708, 2013.

[72] J.F. Rodriguez, C. Ruiz, M. Doblaré, and G. Holzapfel. Mechanical stresses in abdominal aortic aneurysms: influence of diameter, asymmetry, and material anisotropy. *J Biomech Eng*, 130(2):021023, 2008.

[73] A. Romo, P. Badel, A. Duprey, J.P. Favre, and S. Avril. In vitro analysis of localized aneurysm rupture. *J Biomech*, 47(3):607–16, 2014.

[74] T. Schmidt, D. Balzani, and G.A. Holzapfel. Statistical approach for a continuum description of damage evolution in soft collagenous tissues. *Comput Methods Appl Mech Eng*, 278:41–61, 2014.

[75] J.C. Simo and J.W. Ju. Strain- and stress-based continuum damage models–I. formulation. *Int J Solids Struct*, 23(7):821–40, 1987.

[76] Z. Teng, D. Tang, J. Zheng, P.K. Woodard, and A.H. Hoffman. An experimental study on the ultimate strength of the adventitia and media of human atherosclerotic carotid arteries in circumferential and axial directions. *J Biomech*, 42(15):2535–9, 2009.

[77] O. Trabelsi, F.M. Davis, J.F. Rodriguez-Matas, A. Duprey, and S. Avril. Patient specific stress and rupture analysis of ascending thoracic aneurysms. *J Biomech*, 48(10):1836–43, 2015.

[78] O. Trabelsi, A. Duprey, J.P. Favre, and S. Avril. Predictive models with patient specific material properties for the biomechanical behavior of ascending thoracic aneurysms. *Ann Biomed Eng*, 44(1):84–98, 2016.

[79] A. Valentín, J.D. Humphrey, and G.A. Holzapfel. A finite element-based constrained mixture implementation for arterial growth, remodeling, and adaptation: theory and numerical verification. *Int J Numer Method Biomed Eng*, 29(8):822–49, 2013.

[80] K. Volokh. Prediction of arterial failure based on a microstructural bi-layer fiberâĂŞmatrix model with softening. *J Biomech*, 41(2):447–53, 2008.

[81] K. Volokh. Cavitation instability as a trigger of aneurysm rupture. *Biomech Model Mechanobiol*, 14(5):1071–9, 2015.

[82] W.W. von Maltzahn, D. Besdo, and W. Wiemer. Elastic properties of arteries: a nonlinear two–layer cylindrical model. *J Biomech*, 14(6):389–97, 1981.

[83] D.A. Vorp, B.J. Schiro, M.P. Ehrlich, T.S. Juvonen, M.A. Ergin, and B.P. Griffith. Effect of aneurysm on the tensile strength and biomechanical behavior of the ascending thoracic aorta. *Ann Thorac Surg*, 75(4):1210–4, 2003.

[84] T. Waffenschmidt, C. Polindara, A. Menzel, and S. Blanco. A gradient–enhanced large-deformation continuum damage model for fibre–reinforced materials. *Comput Methods Appl Mech Eng*, 268:801–42, 2014.

[85] H.M. Wang, X.Y. Luo, H. Gao, R.W. Ogden, B.E. Griffith, C. Berry, and T.J. Wang. A modified holzapfel-ogden law for a residually stressed finite strain model of the human left ventricle in diastole. *Biomech Model Mechanobiol*, 13(1):99–113, 2014.

[86] A. Wittek, W. Derwich, K. Karatolios, C.P. Fritzen, S. Vogt, T. Schmitz-Rixen, and C. Blase. A finite element updating approach for identification of the anisotropic hyperelastic properties of normal and diseased aortic walls from 4D ultrasound strain imaging. *J Mech Behav Biomed Mater*, 58:122–38, 2016.

[87] S.L. Woo, J.A. Weiss, M.A. Gomez, and D.A. Hawkins. Measurement of changes in ligament tension with knee motion and skeletal maturation. *J Biomech Eng*, 112(1):46–51, 1990.